This project has received funding from the European Union's Horizon 2020 research and innovation programme under grant agreement No 871813.

ICT Project No 871813

MUNDFAB

Modeling Unconventional Nanoscaled Device FABrication

D2.1: First batch of experimental results on heated implants and SPER

P.L. Julliard (STM/CNRS), R. Monflier (CNRS),
R. Demoulin (CNRS), R.P. Dumas (STM), F. Monsieur (STM),
F. Hilario (STM), S. Joblot (STM), D. Rideau (STM),
A. Hemeryck (CNRS), F. Cristiano (CNRS)

29/09/2021

Quality management

This deliverable was reviewed by:

Anne-Sophie Royet (CEA-LETI)

Ioannis Deretzis (CNR-IMM)

Contents

Abstract

In this deliverable, we report the results of our investigations about the impact of the wafer temperature on the residual damage remaining after an ion implantation process, as well as on the defects formed during a subsequent annealing step. We first showed that the substrate self-induced heating during Carbon implantation has a strong impact on the thickness of the induced amorphous layers. The role of a specific machine-related parameter (i.e. the backside pressure cooling) on the control of this phenomenon was understood and successfully modeled by a combination of a “homemade” model with the KMC simulation code Sentaurus Process.

Then we discuss the case where the wafer substrate is deliberately kept at a high temperature during the implant. For a “heated implant” of Arsenic in Silicon, we show that when the implant temperature is increased from RT to 150°C, an enhanced point defect annihilation occurs during the implant, which prevents the formation of a continuous amorphous layer, while still leaving a considerable level of damage. A further increase of the implant temperature up to 500°C results in an almost perfect structure, with no evidence of amorphous or highly damaged regions. TEM and photoluminescence techniques were performed after thermal anneal of the implanted samples. It is found that the optical emission peaks detected by photoluminescence spectroscopy do not originate from the extended defects observed by TEM, but rather from small interstitial clusters formed during the annealing, whose size is below the TEM detection limit. In contrast, in the case of the high-energy Phosphorus implants, a direct correspondence between the photoluminescence emission peaks and the observed elongated dislocations was established.

Finally, we describe the full set of new experiments planned for tasks T2.1 and T2.2, which will be performed, in collaboration with the privileged partner AMAT, on the dedicated SiGe wafers fabricated by LETI.

1 Introduction

The results presented in this deliverable are related to the experimental activity carried out in tasks 2.1 and 2.2 of the MUNDFAB project, whose main objective is to develop models for the description of low thermal source/drain fabrication processes. In the case of Ion Implantation-based processes, two approaches are investigated: *(i)* non-amorphizing implants where the as-implanted damage is reduced by performing the implants at temperatures above room temperature (RT) (and below 500°C), i.e. “heated implants” (Task 2.1) and *(ii)* amorphizing RT implants followed by low temperature Solid Phase Epitaxial Regrowth (SPER, Task 2.2).

Due to the delay in the fabrication of dedicated wafers for the implementation of the initially planned experiments (cf. Deliverable D3.2), the results presented in the first three sections of this document are based on implanted Silicon wafers that were available at STMicroelectronics at the beginning of the project. They cover the investigation of self-induced heating during Carbon implantation (section 1) and the damage evolution during heated implants of Arsenic (section 2) and Phosphorus (section 3).

Finally, since the dedicated SiGe wafers have been fabricated by LETI, the planned experiments for tasks T2.1 and T2.2 have been designed. They will be presented in the final section of this report (section 4).

2 Self-induced heating by C^+ implantation

2.1 Implant temperature and damage evolution

Ion implantation is typically used to introduce dopants into silicon devices. One of its drawbacks is due to the collisions between the implanted ions and the silicon lattice atoms that can lead to the creation of clusters composed of Si self-interstitials and vacancies, and known as amorphous pockets. Under specific implant conditions, the accumulation of amorphous pockets can lead to the creation of a continuous amorphous layer in the material. The ion implant step is typically followed by a thermal annealing process with the aim to move the implanted ions in substitutional positions. When a continuous amorphous layer is formed, the annealing process results in a perfect recrystallization of the amorphous layer. This phenomenon is named Solid Phase Epitaxial Regrowth (SPER) [1]. It leaves Si self-interstitials in excess below the initial amorphous/crystalline interface. These residual interstitials can evolve into extended defects such as {311} rod-like defects or dislocation loops during the annealing process depending on their concentration and their distance to the surface [2]. Dislocation loops and {311}s can have an impact on the reliability of the subsequently fabricated devices. Indeed, these extended defects can induce dark currents in CMOS imager devices [3]. The evolution of the extended defects population during further annealing (i.e. density and mean size) can also lead to a spreading of the dopant profile by means of the transient enhanced diffusion (TED) [4]. Both amorphizing and non-amorphizing implants need an accurate simulation of the amorphous pockets kinetics to correctly describe the defects present in the final device.

The growth kinetics of amorphous pockets depends on several parameters such as the dose rate of the implant, the ion energy, the ion mass, and the wafer temperature [5]. Among these different parameters, the wafer temperature is particularly difficult to control, as it can dynamically increase during the implant due to the collisions between the ions and the silicon lattice.

Industrial implanters generally include a cooling system to prevent the wafer to reach temperatures high enough to damage the resist [6], while the total dose is achieved by several implant steps to avoid a constant flux of ions on the wafer and hence reduce the heating process. Moreover, the ion beam (with the shape of a ribbon) is scanned over the entire wafer surface so that only a limited region is exposed to the beam at a given time during the process. This method allows each implanted area of the wafer to cool down between two subsequent implant steps and produces a less significant heating compared to that produced by an equivalent continuous implant. However, even if the temperature is maintained below a harmful level thanks to these technological solutions, a self-induced heating still occurs during the implant, which can affect the amorphous pockets growth kinetics.

Based on these observations, reliable predictive models must be developed in order to:

- determine the relation between self-induced heating and amorphous pockets kinetics
- predict the wafer temperature evolution as a function of the implant machine parameters.

The simulation software used to achieve these objectives and presented in this section is a Kinetic Monte Carlo software (KMC) developed by Synopsys (Sentaurus Process [7]) coupled to a homemade code for temperature evolution. This choice combines the simulation efficiency of a robust commercial simulator for defect generation to the flexibility of a homemade code for the integration of the machine parameters in the calculation.

2.2 Implant tool

The implant tool used for this study is an industrial Viista HCS implanter by Applied Materials, specifically designed for low energy implants. The end-station of the Viista HCS is represented in Fig. 1. Ions are implanted by means of a fixed ribbon beam placed in front of the wafer, which moves back and forth in front of it. The full implant dose is achieved by N_{passes} (back or forth) of the wafer. Ions are accelerated and hit the wafer with an energy E_{ions}. The flux of ions hitting the wafer is given by the intensity I_{beam}. The cooling system consists of a N_2 gas in contact with the wafer. The gas itself is cooled down by an internal water system. Velocity of the wafer, width of the ribbon beam and number of steps N_{passes} are not the same from one process to another. These parameters are optimized by the implanter for each implant depending on the requested ion energy and dose.

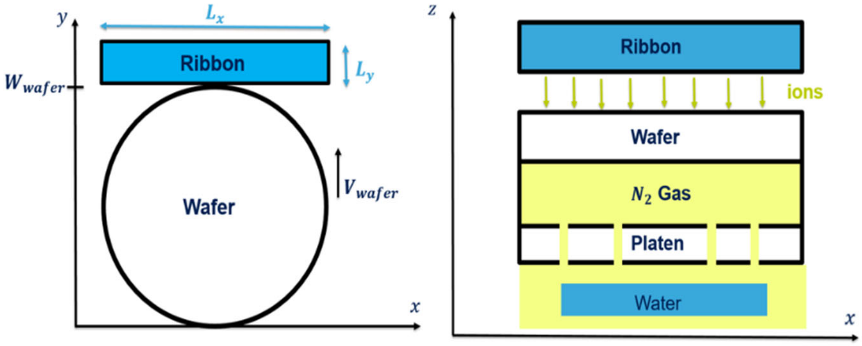

Fig. 1: Schematics of the implanter end-station used in this work (left) and of its cooling system (right).

2.3 Model for implantation self-heating

The temperature evolution of one unit area at the center of the wafer is calculated in our model. This area is alternatively heated and cooled down, depending on whether it is exposed to the beam or not. The first step for the estimation of the temperature profile of such unit area is then to calculate the time during which the beam is above the area and the time interval between two consecutive beam exposures. The velocity of the moving wafer is measured by the implanter sensors. The wafer diameter, W_{wafer}, being known, it is therefore possible to calculate the beam exposure time, $t_{exposed}$, and the time between two consecutive exposures, $t_{cooling}$:

$$t_{exposed} = \frac{L_y}{V_{wafer}} \quad (1) \quad \text{and } t_{cooling} = \frac{W-L_y}{V_{wafer}} \quad (2)$$

The temperature profile is then calculated using the one-dimensional heat equation:

$$d_w \rho c_p \frac{dT}{dt} = -\alpha p_{cooling}\left(T - T_f\right) + P_{beam}(t) \quad (3)$$

This equation assumes that the wafer is thin enough (d_w being the wafer thickness) to be uniformly heated along its depth while being exposed to the beam. It also assumes that the heat dissipation along the x and y axes can be neglected compared to the heat exchanges with the surface in contact with the cooling system. The power of the beam per unit area $P_{beam}(t)$ is equal to $\frac{E_{ions}*I_{beam}}{qA}$ for a heating phase and is null for a cooling phase. The remaining parameters are defined as follows: ρ and c_p are the silicon mass density and thermal capacitance, T_f is the water temperature (cf. Fig. 1), $p_{cooling}$ is the cooling gas pressure and α (m s^{-1} K^{-1}) is a constant.

The temperature evolution calculated according to eq. (3) by our homemade code is expected to exhibit a saw-tooth like increase. An example is shown in Fig. 2 (details will be discussed in next section). In a second step, our code generates a KMC input file containing the information about the temperature time evolution, which is transferred to the Sentaurus Process KMC software for the simulation of the ion implant step. The implantation process is divided in N_{passes} and each implantation step is simulated at a temperature determined at the end of the previous one.

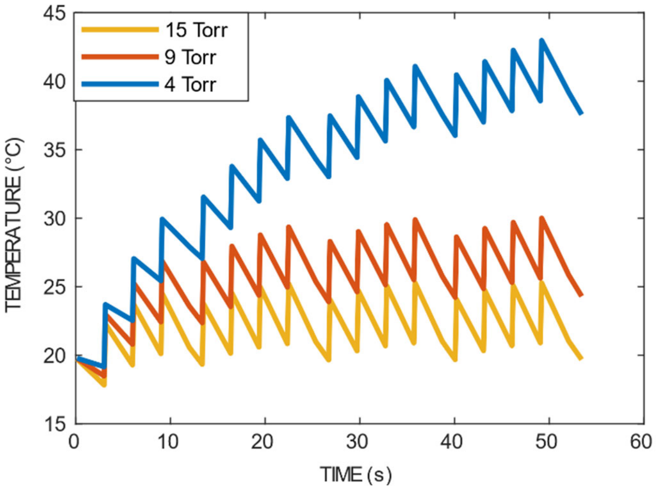

Fig. 2: Simulation of temperature evolution during a 60 keV carbon implant with a dose of $1.5\ 10^{15} cm^{-2}$ *for three different cooling pressures (4, 9 and 15 Torr).*

Atomic diffusion steps are included between successive implant steps in the KMC input file to simulate the defect evolution in the wafer when the area is not irradiated by the ribbon ion beam. Finally, dose rate is also implemented in the KMC input file, which is defined as the ion dose received per unit time by a given area during the time interval at which the area is exposed to the ribbon beam.

2.4 Experimental method

The validation of our self-heating model has been achieved by comparison with experimental results. The parameter used for the comparison is the thickness of the continuous amorphous layer created by a carbon implant. Indeed, amorphous pockets are too small to be reliably observed and measured whereas a continuous amorphous layer can be simply measured by TEM due to the different contrast of the amorphous and crystalline phases in TEM images. Moreover, the amorphization kinetics is not the same for heavy and light ion implants. For a light ion implant, an amorphous layer is created by the accumulation and growth of small amorphous pockets whereas a single heavy ion can directly create a stable amorphous area around its collision cascade. Amorphization by light ions is therefore more sensitive to a modification of the implant temperature and this justifies the choice of carbon for our model validation.

In order to isolate the impact of the wafer temperature on the amorphization from other experimental parameters, fixed implant energy and dose were used for the experiment, while the backside cooling pressure was varied. Indeed, the implanter fixes the ribbon beam dimension, the number of implantation step and the velocity of the wafer depending on the chosen dose and the energy of the implant. The temperature modification of the wafer therefore occurs at fixed heating and cooling time intervals, the differences in the temperature levels only being due to the different cooling pressures used.

For this experiment, the ion energy was fixed at 60 keV, while the ion dose was set at 1.5×10^{15} cm^{-2}, which is close to the threshold value for amorphization in the case of a room temperature implant. Indeed, close to this threshold, light mass ions exhibit a super-linear behavior in the damage accumulation as a function of temperature. Implantation of a light ion such as carbon in this super-linear regime therefore makes the system very sensitive to changes in temperature, which are expected to result in easily observable changes in damage formation.

Fig. 2 reports the simulated temperature profiles for a Carbon implant performed at 60 keV and to a dose of 1.5×10^{15} cm^{-2}, using a cooling pressure of 4, 9 and 15 Torr, respectively. The results clearly indicate that the lowest cooling pressure leads to the higher wafer temperatures.

2.5 Experimental and simulation results

Figure 3 (right, A, B and C) reports the TEM cross section images taken from silicon samples implanted with 60 keV C^+ to a dose of 1.5×10^{15} cm^{-2} for three different cooling pressures (15, 9 and 4 Torr, respectively). The TEM images clearly show that an amorphous layer is formed in the three samples, as indicated by the uniform light contrast regions visible in all images below the surface (indicated by a red arrow in image B). However, its thickness varies depending on the backside cooling pressure used for the implant. In particular it decreases when the cooling pressure decreases, i.e. when the wafer temperature increases (cf. Fig. 2). This result already provides a qualitative explanation about the impact of the self-induced heating on damage generation. Indeed, the increased temperature favors the point defect recombination and hence slows down the amorphization process.

To enable the quantitative comparison between the experimental observations and the model predictions, the experimental values of the amorphous layer thickness have been determined by plotting the depth profile of the image contrast from each TEM micrograph. The contrast level at a given depth is obtained by laterally integrating the signal over the entire image. At a given depth on the sample the silicon is considered as amorphous where the brightness is above 85% of the brightest point in the TEM image.

The extracted values are reported in Table I and compared with those obtained with the KMC simulation code, which enables to plot average 1-D depth profiles of the point defects generated during the implant. The threshold value for amorphization is set at a point defect concentration of $1.5\ 10^{22}\ cm^{-3}$. This enables amorphization 1-D profiles along the depth of the wafer, which are presented in Fig. 3 (left) for the three different values of the gas cooling pressure. The simulated curves indicate the same trend as for the experimental results, i.e. the amorphous thickness increases proportionally to the backside cooling pressure. The amorphous layer thickness reaches 120 nm with a backside cooling pressure of 15 Torr, whereas an amorphous layer of 80 nm is obtained for a backside cooling pressure of 4 Torr. The simulated values are in very good agreement with the measured ones, as shown in Table I, therefore demonstrating the reliability of the physical model developed for their calculation.

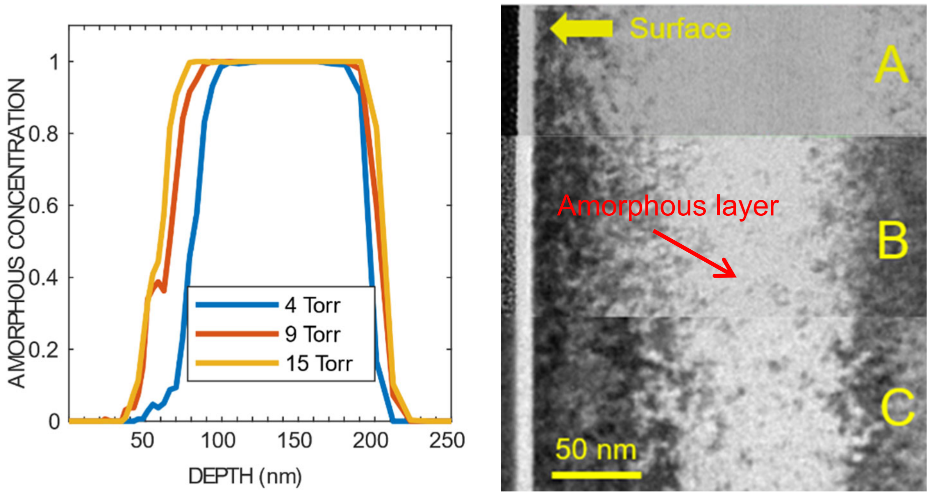

Fig. 3: (Left) Simulation of amorphous concentration as function of the depth for a 60 keV carbon implantation with a dose of $1.5\ 10^{15}\ cm^{-2}$ and for cooling pressures of 15, 9 and 4 Torr. (Right) A, B and C are the TEM images of 60 keV carbon implanted wafers with a dose of $1.5\ 10^{15}\ cm^{-2}$ and a cooling pressure of 15, 9 and 4 Torr respectively.

Amorphous layer thickness (nm)		
Wafer	***KMC***	***Experimental***
Carbon 60 keV $1.5\ 10^{15} cm^{-2}$ 4 Torr	80	80
Carbon 60 keV $1.5\ 10^{15} cm^{-2}$ 9 Torr	103	100
Carbon 60 keV $1.5\ 10^{15} cm^{-2}$ 15 Torr	120	110

Table I: Comparison between simulation and experimental data for amorphous layer thickness.

The effect of the cooling pressure on amorphization was also simulated for a reduced Carbon implant energy (30 keV) compared to the previous case, while the implant dose was increased up to 2x10^{15} cm^{-2}. The difference in temperature for the two implantation conditions can be observed in Fig. 4 (left). The effect of the pressure is the same as for the 60 keV implantation: a smaller cooling pressure induces higher temperature during implantation. Amorphization profiles for these two conditions are simulated in Fig. 5 (center). They follow the same trend as in the 60 keV implant case, i.e. the higher the cooling pressure, the thicker the amorphous layer. However, the difference between the amorphous thicknesses calculated with the two gas pressures is much smaller compared to the previous case. Still, the TEM images allow to confirm the reliability of the calculations by showing more crystalline areas near the surface (and hence a thinner amorphous layer) for the high-pressure case (Fig. 4, right, image B).

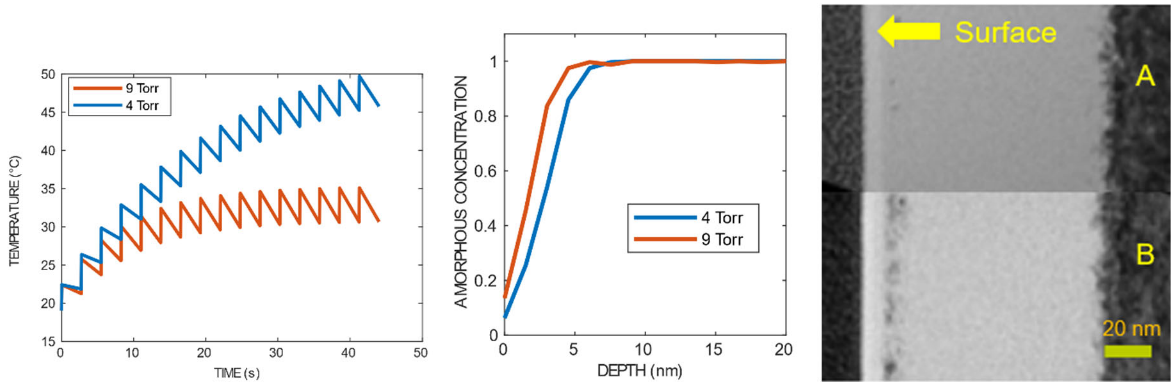

Fig. 4: (Left) Simulation of temperature evolution during a 30 keV carbon implant with a dose of $2\ 10^{15}cm^{-2}$ *for three different cooling pressures (4, 9 and 15 Torr). (Center) Simulation of amorphous concentration as function of the depth for a 30 keV carbon implantation with a dose of* $2\ 10^{15}\ cm^{-2}$ *and for cooling pressures of 9 and 4 Torr. (Right) A and B are the TEM images of 30 keV carbon implanted wafers with a dose of* $2\ 10^{15}\ cm^{-2}$ *and a cooling pressure of 9 and 4 Torr respectively.*

Finally, we tested the simulation model in the high dose regime (4x10^{15} cm^{-2}) i.e. well beyond the amorphization threshold, where the wafer temperature is expected to have an even weaker impact on the amrophisation kinetics. The simulation results are shown in Fig. 5. for an implant energy of 30 keV and cooling pressures of 4, 9 and 15 Torr. A difference in wafer temperature is still observed (cf. Fig. 5 left), which is even larger than in the previous lower dose implants, however, the KMC simulations do not predict any significant difference in the amorphous thickness, in perfect agreement with the TEM images (Fig. 5 right).

In summary, this work shows that the amorphous thickness can be finely tuned from dozens of nm to less than 5 nm by changing a specific machine-related parameter (i.e. the backside pressure cooling) on a standard industrial implanter. Moreover, the combination of a “homemade” model (for the prediction of the wafer temperature as a function of this specific machine-related parameter) with the KMC simulation code Sentaurus Process (for the evolution of implant-induced damage and amorphous pockets kinetics) results in a perfect prediction of the observed amorphization kinetics in a wide range of implant conditions, including those corresponding to the super-linear regime (close to the amorphization threshold) as well as the high-dose implants (full amorphization).

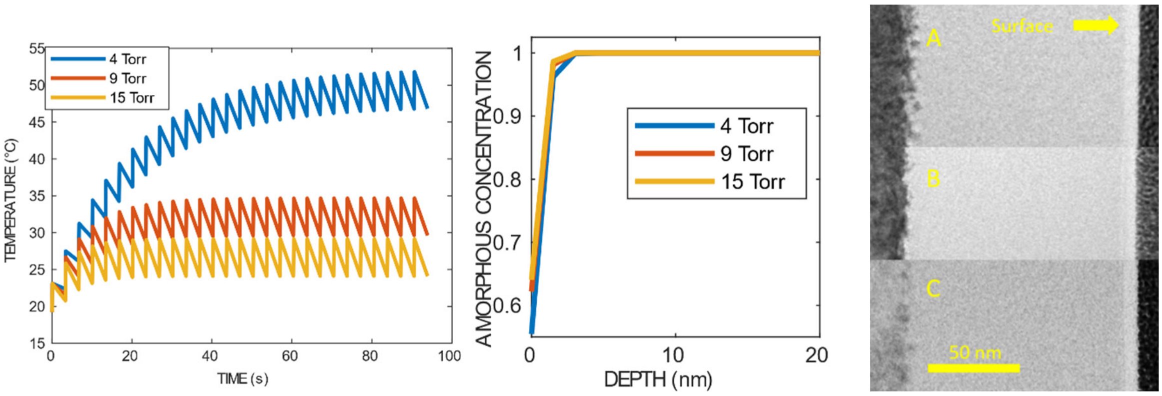

Fig. 5: (Left) Simulation of temperature evolution during a 30 keV carbon implant with a dose of $2\ 10^{15} cm^{-2}$ *for two different cooling pressures (4, 9 Torr).(Center) Simulation of amorphous concentration as function of the depth for a 30 keV carbon implantation with a dose of* $4\ 10^{15}\ cm^{-2}$ *and for cooling pressures of 4, 9 and 15 Torr. (Right) A, B and C are the TEM images of 30 keV carbon implanted wafers with a dose of* $4\ 10^{15}\ cm^{-2}$ *and a cooling pressure of 15, 9 and 4 Torr respectively.*

3 Arsenic heated implants

3.1 Industrial context

The optimization of npn SiGe Heterojunction Bipolar Transistors requires the continuous improvement of the transition frequency and the maximum oscillation frequency [8]. A possible solution to fulfill both requirements consists in decreasing the base-collector resistivity and the base-collector capacitance. A compromise can be achieved by doping the collector through a high dose implantation at medium energy [9]. However, in the case of Arsenic doping, such conditions may introduce a high level of damage in the wafer. Upon subsequent annealing, typically performed at medium temperatures (700°C-800°C) for long times, the implantation-induced damage is expected to evolve into extended defects, which can be responsible for dopant profile modification through Transient Enhanced Diffusion (TED) [10]. Moreover, extended defects located in the space charge region can also be a source of deterioration of electrical performances. In order to minimize the defects formation process, while keeping the required high dose/medium energy implant conditions, ion implantation performed at high temperature is investigated as a possible solution. Indeed, as seen in the previous section, the self-induced temperature increase during the implant promotes recombination of interstitial and vacancies in amorphous pockets and hence reduces the overall implantation-induced damage. An alternative, more effective, method consists in intentionally increasing the wafer temperature by placing it on a heating chuck during the implant.

3.2 Experimental details

Such “heated” implants (HT implants in the following) have been investigated within the MUNDFAB project with the aim of establishing a correlation between the implant temperature and the residual defects population in terms of their crystallographic structure (as determined by TEM analysis) and their optical properties (investigated by means of Photoluminescence imaging and spectroscopy). To this purpose, three silicon wafers have been implanted with As ions as described in Table II. A double implant step has been used, in agreement with technologically relevant recipes being tested at STM. All wafers have been implanted with the same ion energies and doses, the only difference being the implant temperature: room temperature (RT), 150°C and 500°C.

Sample name	Implant temp. (°C)	Ion energy (keV)	Arsenic Dose (cm^{-2})
As 12	20 (RT)	180 + 100	$1x10^{14}$ + $8x10^{13}$
As 15	150		
As 18	500		

Table II: Arsenic implantation doses, energies and temperatures used during implantation.

Similarly to the implant conditions, the annealing recipe has been defined according to the process developments carried out at STM. The multiple-step annealing process is described in Table III and was applied to all the implanted samples.

Annealing stpes	Temperature (°C)	Time
1	625	2h
2	750	1h
3	700	3h30
4	625	52 mn
5	800	30 mn
6	750	1 h

Table III: Annealing process performed after As implantation.

The results obtained in this work have been used as an experimental reference for the development and calibration of “heated” implants KMC simulation models, that will be reported in deliverable D2.3.

3.3 Results

3.3.1 TEM analysis

Figure 6 presents the cross-section TEM images taken from samples implanted at different implant temperatures and prior to the annealing step. It is evident that the residual damage remaining after the implant strongly depends on the implant temperature. At room temperature (Figure 6 left), a continuous buried amorphous layer is formed, as indicated by the uniform light contrast region located below the surface and indicated by the green vertical lines in the figure. Its thickness is of ~140 nm. When the implant temperature is increased up to 150°C (Figure 6, center), no continuous amorphous layer is formed, however a highly damaged buried layer is observed within an otherwise crystalline material, which extends from a depth of ~40 nm down to ~150 nm. This clearly indicates that, thanks to the higher implant temperature, an enhanced point defect annihilation occurs during the implant (compared to the RT case), which prevents the formation of a continuous amorphous layer, while still leaving a considerable level of damage. Finally, the crystalline quality of the sample implanted at 500°C (Figure 6, right) is almost perfect, with no evidence of amorphous or highly damaged regions. If any defects clusters or amorphous pockets are still formed in this case, their size is therefore below the detection limit of the TEM analysis.

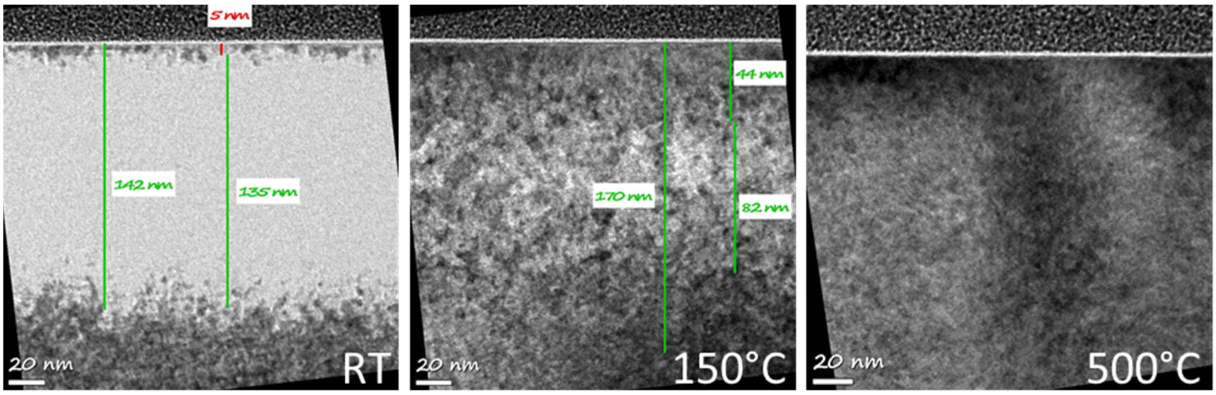

Figure 6: Cross section TEM micrographs taken from samples implanted with As (cf. Table II for implant details) at different implant temperatures: room temperature (left), 150°C (center) and 500°C (right)

The differences in the nature and spatial extension of the residual damage observed in the as-implanted samples is expected to have a strong impact on the extended defects formed during the annealing step. After annealing (carried out according to the recipe described in Table III), the three samples were observed again in both cross-section (Figure 7) and plan-view (Figure 8) configuration.

In the cross section image of the sample implanted at room temperature (cf. Figure 7 left), a double layer of extended defects (loop-like contrast) is clearly observed. Such double layer is consistent with the formation of a buried amorphous layer after the implant containing two a/c interfaces [11]: the lower defect layer corresponds to the end-of-range defects formed below the deeper a/c interface, while the upper one is probably related to the defects formed when the two advancing a/c interfaces meet during regrowth (type IV defects in [11]). The end-of-range defects formed below the deeper a/c inteface are due to the excess Si interstitial atoms remaining on the crystalline side of the interface [12] and are clearly identified thanks to plan-view TEM analysis (Figure 8 left). In this particular sample, they mainly consist of faulted dislocation loops lying on {111} planes.

The cross-section and plan-view TEM images relative to the sample implanted at 150°C are shown in Figures 7 (center) and Figure 8 (center), respectively. In this case, a single layer of dislocation loops is observed after the anneal, extending from a depth of ~70 nm down to ~150 nm. Indeed, in the case of a subamorphizing implant, a single layer of defects is expected to form in the vicinity of the ion mean projected range, i.e. at a depth where the highest level of damage is produced (Type I defects [11]). This is confirmed by SIMS depth profile of the as-implanted sample (not shown), showing that the As concentration peak is located at a depth of 75 nm.

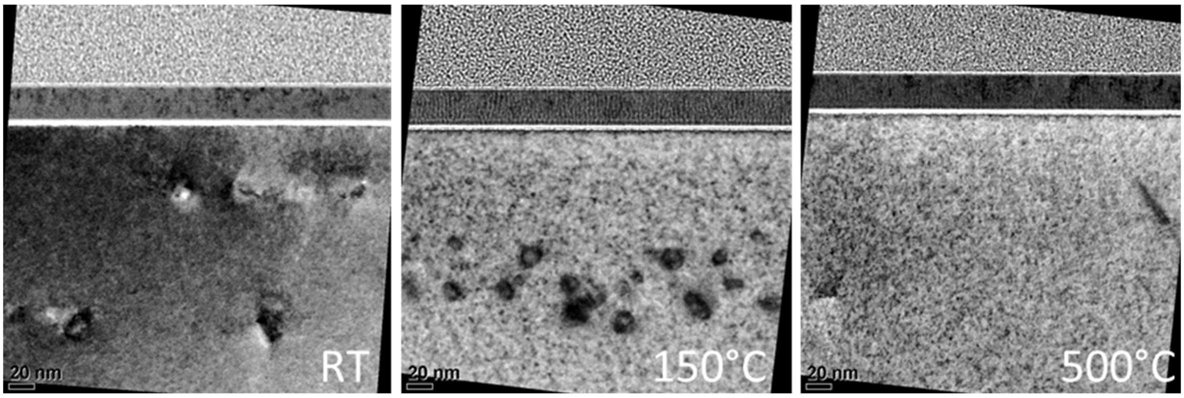

Figure 7: Cross section TEM micrographs taken from samples implanted with As (cf. Table II for implant details) and annealed according to Table III. The As implants were carried out at different temperatures: room temperature (left), 150°C (center) and 500°C (right)

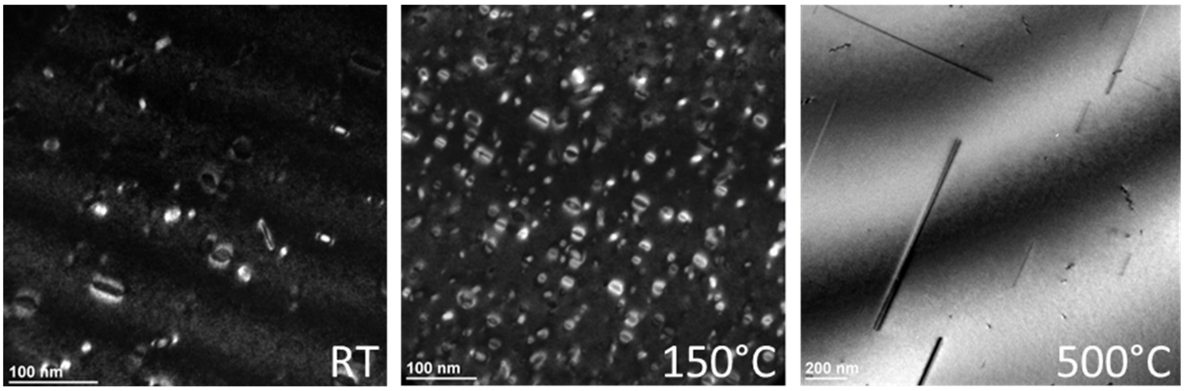

Figure 8: Plan view TEM micrographs taken from samples implanted with As (cf. Table II for implant details) and annealed according to Table III. The As implants were carried out at different temperatures: room temperature (left), 150°C (center) and 500°C (right)

Finally, Figure 7 (right) and Figure 8 (right) report the TEM images relative to the sample implanted at 500°C. Despite the apparent absence of residual damage after the implant (cf. Figure 6 (right)), extended defects are observed after the anneal. Their density is low compared to the samples implanted at RT or 150°C (only two defects visible in the cross section image of Figure 6 right), which makes it difficult to determine a reliable “average” location of the defect layer. However, considering that no amorphization occurred in this sample (i.e. similarly to the sample implanted at 150°C), the observed defects are to be associated to the peak of the implant induced damage, located near the ion mean projected range. Moreover, the much lower level of residual damage of the sample implanted at 500°C seems to have a strong impact on the crystallographic nature of the extended defects formed during the anneal. Indeed, in this case, the defects consist of extremely long (several hundreds of nm) {311} rod-like defects, while no circular dislocation loops were observed (cf. Figure 8 (right)).

This result is consistent with the lower residual damage observed in this sample with respect to the one implanted at 150°C. Indeed, the defects formed during annealing are known to evolve from small clusters to {311} rod-like defects up to dislocation loops following an Ostwald ripening mechanism [12]. The defect evolution is controlled by few key parameters, including the thermal budget (temperature and duration of the anneal), the vicinity of a highly recombining surface (or interface) and the total amount of Si interstitial atoms, Si_{int}s, generated by the implant and available at the beginning of the anneal. In our case, the first two parameters are the same for whole sample series, the only difference coming from the reduced Si_{int}s population for the sample implanted at 500°C. We can therefore reasonably suppose that, because of such reduced $Si_{int}s$ population, the density of the {311} defects formed in the sample implanted at 500°C is too low to sustain a high exchange rate of $Si_{int}s$ during the anneal, therefore preventing the eventual transformation of the {311} defects into more stable dislocation loops. In order to validate (or contradict) this scenario, the planned action for this activity will therefore be twofold. On the one hand, a detailed TEM-based quantitative analysis of the extended defects formed during annealing will be performed (defect average size, density, and number of $Si_{int}s$ stored in the defects). On the other hand, KMC and continuum models will be implemented to simulate both the damage generation during RT/HT implants and the formation and evolution of extended defects during the anneal.

3.3.2 Photoluminescence Imaging

The three samples implanted at different temperatures were also analyzed by photoluminescence imaging, a non-destructive optical characterization technique available at STMicroelectronics [13], specifically developed to be compatible with industrial manufacturing environment. In particular, PL imaging allows detecting defect-related PL emission peaks at room temperature, which is extremely difficult with conventional PL spectroscopy, due to thermal broadening. In contrast, all the wavelengths contained in the selected range are integrated to enhance the signal to noise ratio, so that the specific information on the energy levels associated to the emitting defects is lost. In addition, the spatial resolution is limited by the minimum size of the detecting pixels (0.275 μm x 0.275 μm). Still, for sufficiently large defects, this technique enables an estimation of the density of emitting defects and of their size. Moreover, depending on the intensity of the emitted signal, it is possible to qualitatively separate defects of different nature. This technique has already been shown to successfully detect PL signals from dislocation loops formed by high-energy phosphorus implantation and anneal [13].

Typical PL maps from the three As-implanted wafers are shown in Figure 9. Defects appear as clear spots (with different levels of grey contrast) on a dark background. The analysis of these maps suggests that the apparent density of emitting defects is highest in the sample implanted at room temperature and decreases when increasing the implant temperature, which is in qualitative agreement with the reduction of residual damage in samples implanted at high temperature. Moreover, the intensity of the emitted signal is clearly highest in the sample implanted at 500°C (Figure 9, right), whereas the defects contained in the samples implanted at RT and 150°C exhibit a very similar signal intensity. Again, this result is in qualitative agreement with the TEM observations, which showed that both samples implanted at RT or 150°C exhibited circular dislocation loops, while {311} rod-like defects only were observed in the sample implanted at 500°C.

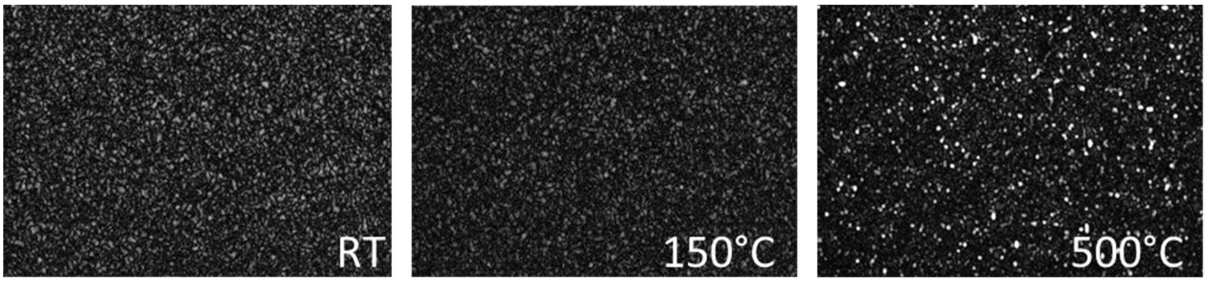

Figure 9: PL imaging maps (120x175 μm area) taken from samples implanted with As (cf. Table II for implant details) and annealed according to Table III. The As implants were carried out at different temperatures: room temperature (left), 150°C (center) and 500°C (right).

3.3.3 Photoluminescence spectroscopy

A more detailed optical investigation of the defects formed in the As implanted samples was finally achieved by photoluminescence spectroscopy, which allows assigning a specific "signature" to each type of defect (energy level, peak width). Photoluminescence spectroscopy is a complementary technique to TEM, especially in the case of extremely small defect clusters composed of few atoms, which cannot be directly observed by TEM.

The photoluminescence experiments were performed with an Oxxius laser diode with a wavelength of 488 nm. This wavelength enables to probe a ~500 nm-thick layer below the surface. The excited area on the wafer has a diameter of 1.2 μm. The power used is 20 mW. Photoluminescence spectra are normalized with respect to the acquisition time. Spectra were acquired at temperatures ranging from 300 K down to 8 K.

Figure 10 shows the PL spectra recorded at 8 K for the samples implanted at three different temperatures. It can be clearly seen that the samples implanted at RT (black curve in Figure 10) and 150°C (red) exhibit a similar behavior. Indeed, they both exhibit a broad peak in the 1300 nm wavelength region (labelled A1 and A3 for the samples implanted at RT and 150°C, respectively), followed by a "shoulder" extending up to ~1400 nm (labelled A2 and A4 for the samples implanted at RT and 150°C, respectively). In contrast, none of these peaks are observed in the sample implanted at 500°C (blue curve in Figure 10), which instead exhibits two peaks in the 1150-1200 nm region. Similarly to the Photoluminescence imaging results showed in previous section, the PL spectroscopy results are again consistent with the TEM observations, which showed that both samples implanted at RT or 150°C exhibited circular dislocation loops, while {311} rod-like defects only were observed in the sample implanted at 500°C.

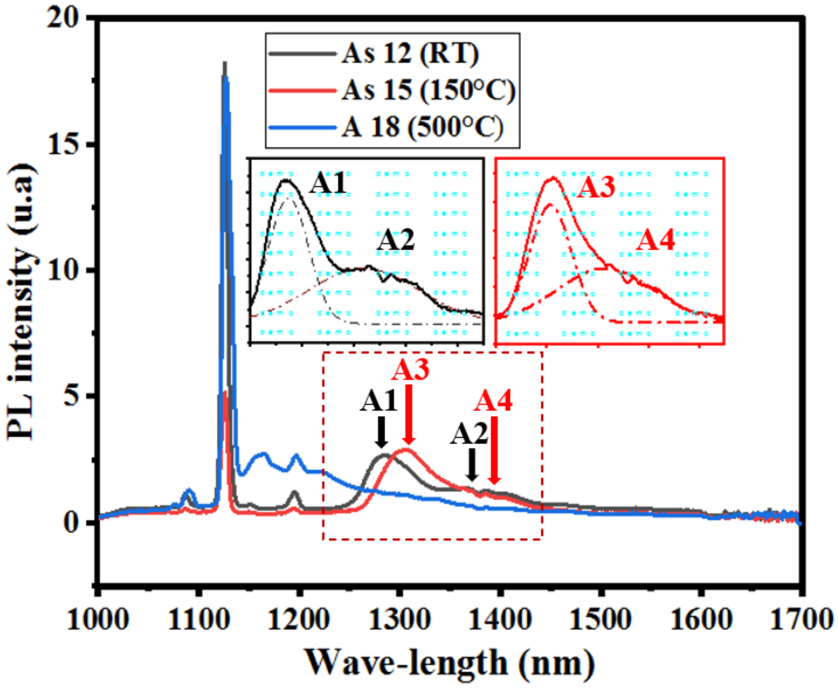

Figure 10: PL spectra taken at a temperature of 8K from samples implanted with As (cf. Table II for implant details) and annealed according to Table III. The As implants were carried out at different temperatures: room temperature, 150°C and 500°C.

We first discuss the PL spectra recorded from samples implanted at RT and 150°C. Deconvolution analysis was applied in order to determine the main optical emission peaks, which are shown in the insets of Figure 10. In both cases the deconvolution of the 8K PL spectra indicates two broad peaks in the same range of wavelength range which are summarized in Table IV.

	RT implant		150°C implant	
Peak label	A1	A2	A3	A4
wavelength (nm)	1287	1358	1303	1357
FWHM (nm)	40	115	41	95
FWHM (meV)	30	84	30	70

Table IV: Peak wavelength positions determined by deconvolution from the samples implanted at RT and 150°C.

The PL spectra acquired at different temperatures from the three implanted samples are reported in Figure 11 (RT and 150°C implants on the left plot, 500°C on the right plot). In all cases, the intensity of the emission peaks is found to decrease when increasing the acquisition temperature, which is expected due to thermal broadening. More importantly, the intensity of the PL spectra of the samples implanted at RT and 150°C (Figure 11 left) decreases in a very similar way, suggesting that the four peaks identified in these samples (A1-A4) have the same origin, i.e. they originate from the same defect type.

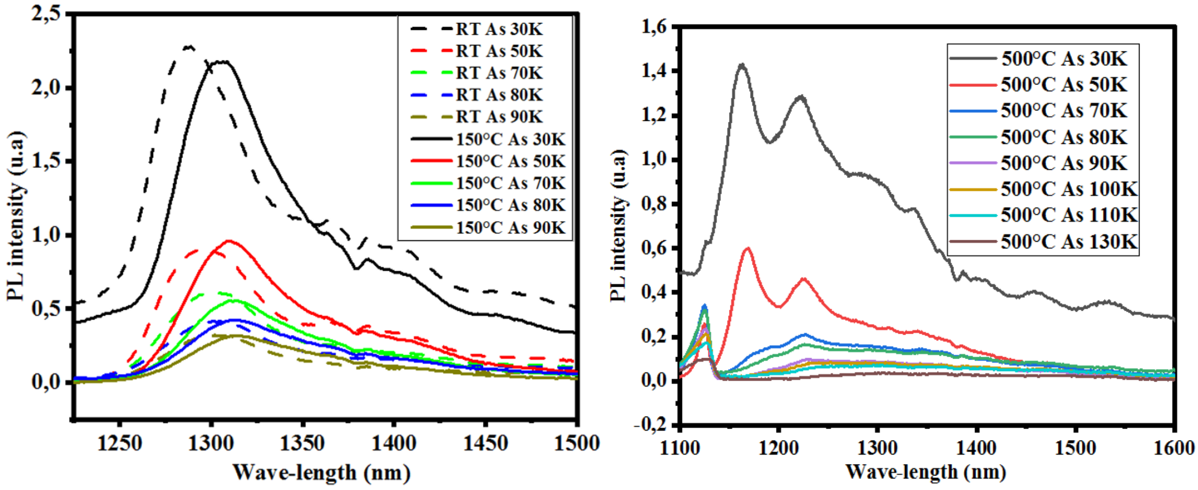

Figure 11: PL spectra acquired at different temperatures from samples implanted with As (cf. Table II for implant details) and annealed according to Table III. The As implants were carried out at different temperatures: room temperature (left), 150°C (left) and 500°C (right).

TEM analysis from the samples implanted at RT and 150°C showed that both samples exhibited circular dislocation loops (cf. Figure 8a and 8b), however none of the observed PL peaks in these samples (A1-A4) correspond to the emission lines typically associated to dislocations in the literature [14]. These are known as D-lines and are generally observed by pairs called D1/D2 and D3/D4 in [14]. In our case, although peaks A1 and A3 are close in wavelength to the D3 line, no peaks are observed near the "coupled" D4 wavelength. In addition, the observed peaks are much broader than the typical D-lines peaks. In fact, D-lines were first observed in samples containing dislocations generated by plastic deformation ([14]

and references therein), which is a different process compared to ion implantation and annealing. Moreover, the presence of contaminants and/or precipitates located in the vicinity of the dislocations has been shown to play an important role in enhancing or reducing their intensity [14][15].

In the case of dislocations induced by ion implantation and annealing, D-lines were observed in the extreme case of a high dose As implant at 1x10^{16} cm^{-2} [16] (i.e. ~50 times higher than the dose investigated in this work) and annealing at temperatures not lower than 900°C (i.e. 100°C higher than the temperature investigated here). In such conditions, both the high density and size of the formed dislocations might explain the appearance of the D-lines in the PL spectra. In contrast, for lower implant doses, many examples exist in which no D-lines were observed by PL in the presence of dislocation loops [17][18], in agreement with our results.

Several other works have investigated the photoluminescence spectra in silicon samples containing implant-induced defects, especially in the case of Si$^+$ ion implants [19][20][21]. In this case, the formation and evolution of the defects, from small clusters to {311} rod-like defects up to dislocation loops is well known [12], and a better correlation with the PL peak evolution is therefore possible. An example is given in Figure 12, taken from ref. [20], which shows the PL spectra obtained from silicon implanted with Si$^+$ ions (300 keV, 3x10^{14} cm^{-2}) and annealed for 30 minutes at different temperatures. At 300°C, the PL spectrum shows sharp X and W peaks at 1193 nm and at 1219 nm (with W phonon replica at 1244 nm), which are associated to small “compact” interstitial clusters (i.e. I_2, I_4,) [19]. At 600°C, the broad S1 and S2 peaks are observed at 1325 nm and 1398 nm. They are likely to be associated with <110>-oriented chains of I-clusters clusters corresponding to the precursors of the {311} rod-like defects. The latter are finally associated to the R-line peak observed at 1372 nm after a 700°C anneal.

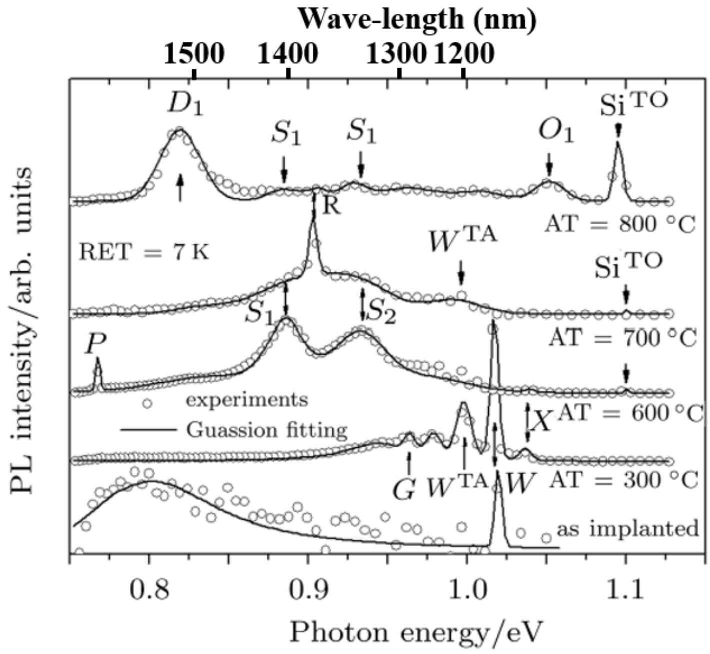

Figure 12: PL spectra obtained in Silicon samples implanted with Si ions and annealed at different temperatures (taken from ref. [20]).

It has to be noted that the S1/S2 peaks are systematically broader than all other observed peaks. The line shape broadening is attributed to the consequence of quantum confinement of carriers in the strain region surrounding the defect [22] (i.e. it is not a signature of the defect itself). For this reason, an “extended” defect configuration (i.e. the “Interstitial chains” structure proposed in ref. [19]) is assumed to explain the observed peak broadening. Interestingly, the “interstitial chain” configuration was also proposed to explain the presence of similar broad PL peaks (located in the same wavelength interval as the S1/S2 peaks) in Si samples implanted with Si ions at doses similar to those investigated here, but annealed at a much higher temperature (1200°C) [17]. In that case, no extended defects were observed in TEM, presumably due to their full dissolution upon high temperature annealing, so that the proposed “interstitial chain” clusters responsible for the broad PL peaks, should be associated to some “residual” defects whose size is below the TEM detection limit.

In this work (cf. Figure 10 and Table IV), the broad peaks observed in the samples implanted with As at RT and 150°C appear in pairs (A1/A2, and A3/A4, respectively). Although they are not located at exactly the same wavelength as the S1/S2 peaks discussed above, they exhibit a very similar width as well as the same wavelength separation. Moreover, the peak evolution as a function of the acquisition temperature (cf. Figure 11 left) is also consistent with that of the S1/S2 peaks. It is therefore suggested that, similarly to S1/S2, the A1-A4 peaks observed in this work also originate from small interstitial defects (i.e. smaller than the TEM detection limit), which are organized in an “extended” fashion (in agreement with the observed peak broadening). Indeed, due to Ostwald ripening [23][24], large defects containing thousands of atoms, such as {311} rod-like defects and dislocation loops can coexist with small interstitial clusters (not visible by TEM) that have not undergone a complete transformation into larger extended structures. In the next reporting period, KMC and continuum simulations will therefore be implemented to calculate the size distribution of all the defects formed during annealing and estimate the residual population of defect clusters whose size is compatible with the observed PL spectra.

We now discuss the PL spectra recorded from the sample implanted at 500°C, in which only long {311} defects were observed by TEM after annealing. As shown in Figure 10 and Figure 11 (right), the PL spectra exhibit several peaks centered at lower wavelengths compared to the samples implanted at RT and 150°C, and ranging from ~1160 nm and ~1340 nm. These are best seen in the spectrum recorded at a temperature of 30 K (cf. Figure 11 right). Especially for the higher wavelength region of the PL spectrum, the probable overlap of several peaks makes the deconvolution procedure difficult. However, it can be seen that, unlike the A1-A4 peaks observed in samples implanted at RT and 150°C, the temperature behavior of the various peaks is not the same. For instance, the peak centered at ~1160 nm, which is the most intense at 30 K decreases more rapidly when the acquisition temperature increases, compared to the peaks centered at higher wavelengths (i.e. the one at ~1220 nm as well as the broader one close to ~1340 nm). This indicates that different defect structures might be at the origin of the observed PL peaks.

As discussed above (cf. Figure 12), {311} defects such as those observed in this sample by TEM are associated to the sharp R-line centered at 1372 nm. In all the experiments supporting this conclusion, the {311} defects were obtained by implanting Si^+ ions into silicon [19][20][21]. In contrast, the {311} defects observed in our study were induced by a dopant impurity implant (phosphorus), while no R-line was observed in the PL spectra. The absence of such “expected” peak might be possibly explained considering that the optical emission is known to be strongly affected (including its suppression) by the presence of contaminants and/or precipitates located in the vicinity of the defects [14][25] or by the defect decoration by dopant impurities [19].

As for the PL peaks observed in the wavelength range 1160-1340 nm, the identification of their origin is more difficult compared to the A1-A4 peaks observed in the samples implanted at RT and 150°C, mainly because of the difficulty in applying deconvolution to extract a reliable set of individual peaks. However, the wavelength range at which the PL peaks are observed is consistent with the "I-band" peaks observed by Giri and coworkers [19] after anneal at 600°C in silicon implanted with Si^+ ions at high energy. These "I-band" peaks were associated to metastable configurations of "*compact but bigger I-clusters*" than I_4 and I_8 and yet smaller than the interstitial chains related to the S1/S2 peaks discussed above. Moreover, the fact that such metastable clusters possess multiple configurations explained the relatively large width of the related optical peaks. With respect to our work, the supposed "intermediate" size of the clusters responsible for the "I-band" PL peaks is in qualitative agreement with the reduced population of silicon interstitials resulting from a 500°C implant, compared to implants performed at RT and 150°C. Again, KMC and continuum simulations are expected to provide further insight on the size distribution of the I-clusters formed during annealing and hence lead to a reliable interpretation of the experimental PL spectra.

4 Phosphorus heated implants

4.1 Industrial context

Implantations used for photodiode junction need specific conditions of implantation. In general, the dopant profile for these devices requires high energy with a low/medium implant dose [13]. Implantation at high-energy increases the number of generated point defects, as well as their depth, leading to a higher probability to form large and stable extended defects during anneal. Within this context, heated implantations are therefore performed with the aim of decreasing the concentration of defects created just after the implantation process. In this work, a 1.3 MeV Phosphorus implantation is investigated. The implantation is performed at two different temperatures: RT and 150°C with doses of $6x10^{13}$ cm^{-2} (or $2x10^{13}$ cm^{-2} in selected samples). Different annealing atmospheres are also investigated.

4.2 Experimental details

Details of the four samples investigated in this study are given in Table V. The reference process is based on an implant dose of $6x10^{13}$ cm^{-2} and an N_2/O_2 annealing atmosphere. For this process, two implant temperatures will be investigated: RT (sample Ph2) and 150°C (sample Ph3). A lower implant dose is also investigated (sample Ph 12). Finally, considering that the presence of oxygen is known to be a precursor for the formation of extended defects such as dislocations loops [26], a control sample annealed in pure nitrogen is also included in the sample list (sample Ph 18).

Sample name	Ion species	Ion energy	Dose	Implant temperature	Annealing
Ph 2	P	1.39 MeV	6E13	RT	3 min 950°C in N_2/O_2
Ph 3	P	1.39 MeV	6E13	150°C	3 min 950°C in N_2/O_2
Ph 12	P	1.39 MeV	2E13	RT	3 min 950°C N_2/O_2
Ph 18	P	1.39 MeV	6E13	RT	3 min 875°C in N_2

Table V: Details of the implant and annealing parameters used for the fabrication of high-energy posphorus implanted structures.

4.3 Results

4.3.1 TEM analysis

TEM analysis was performed on sample Ph2, implanted at room temperature and annealed in a N_2/O_2 atmosphere (cf. Table V). Due to the extremely low defect density contained in this sample, only very few defects could be reliably imaged. An example is given in Figure 13 (left), showing two isolated defects located at depths of 1.6 μm and 2.8 μm, respectively. They are both located well below the mean projected range of the implanted P ions (~1 μm), but still within the high damage region induced by the high-energy implant, where interstitial defects in the form of dislocations are expected to form. High-magnification images of both defects are shown in Figure 13(center) and Figure 13(right), clearly showing that both defects are on (111) planes. Further analysis would be needed to determine the exact nature of these dislocations, however, it can be safely concluded that they result from the agglomeration of the excess interstitial atoms created during the high-energy implant.

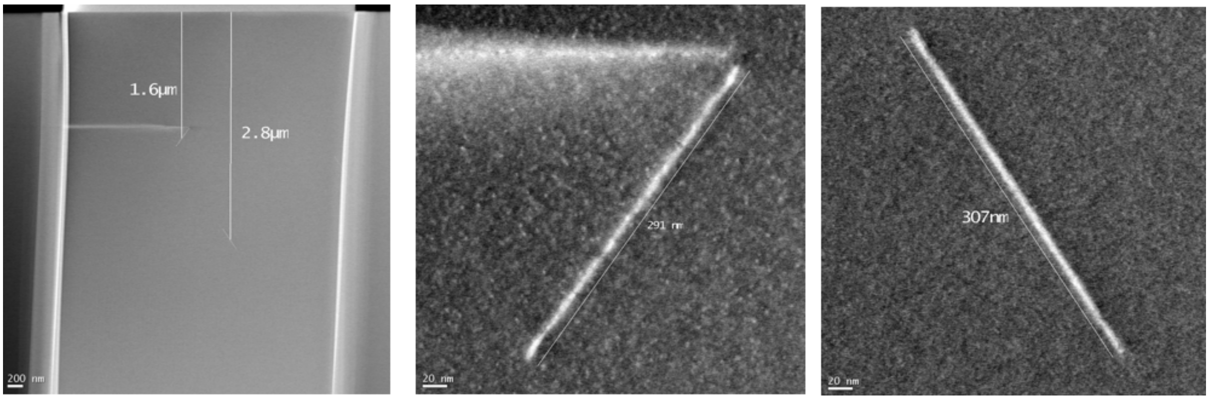

Figure 13: Cross section TEM images from sample Ph 2, implanted at room temperature and annealed in a N_2/O_2 atmosphere (cf. Table V)

4.3.2 Photoluminescence imaging

The photoluminescence imaging method described in previous section was applied to the four investigated samples (cf. Table V) and typical PL maps are shown in Figure 14. Defects appear as clear spots or lines (with different levels of grey contrast) on a dark background. Elongated defects (lines) are systematically parallel to either <100> or <110> directions, and are therefore tentatively related to the dislocations observed in cross-section TEM. Additional defects appear in the form of spots and might be related to shorter (unresolved) dislocations or to defects of a different nature. The impact of the implant temperature can be estimated by comparing the maps reported in the top row of Figure 14 (RT implant on the left, 150°C implant on the right). A decrease of the elongated defects density is clearly visible when the implant temperature is raised to 150°C, which is in perfect agreement with the expected reduction of residual damage in high-temperature implants. Moreover, when the implant dose for a RT implant is decreased from $6x10^{13}$ cm^{-2} (Figure 14 top left) to $2x10^{13}$ cm^{-2} (bottom left), no PL signal is detected. This suggests that the implant damage induced by the low dose implant is fully recovered during the anneal, or that the density of the extended defects is below the detection limit of the technique. Finally, the PL image from the sample implanted at RT with a dose of $6x10^{13}$ cm^{-2} and annealed in pure nitrogen (Figure 14 bottom right) exhibits a higher density of smaller defects compared to the sample implanted in N_2/O_2 (top left). Indeed, during annealing in a N_2/O_2 ambient, it is expected that the interstitial atoms injected due to oxidation strongly contribute to the growth of the extended defects.

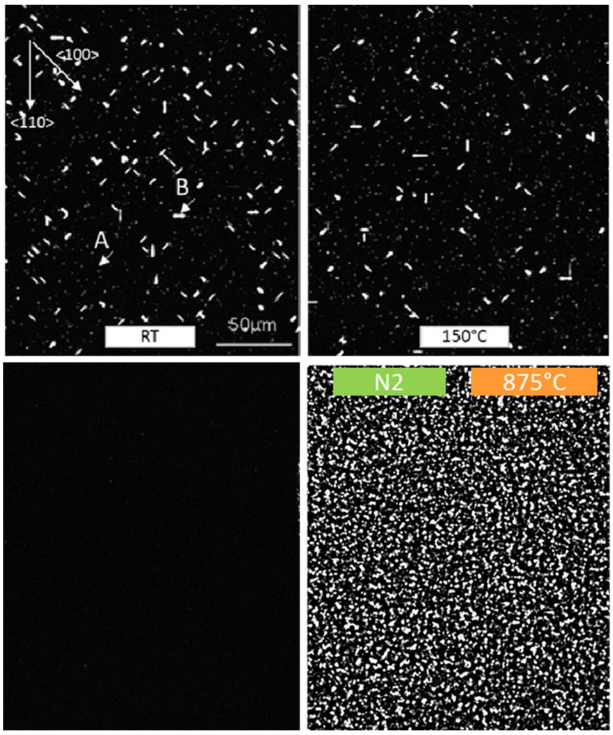

Figure 14: PL imaging maps taken from samples implanted with high-energy P ions with different conditions (cf. Table V). Top left: Sample Ph 2. Top right: Sample Ph 3. Bottom left: Sample Ph 12. Bottom right: Sample Ph 18.

4.3.3 Photoluminescence spectroscopy

PL spectroscopy measurements were carried out using the same setup described in previous section. Figure 15 shows the PL spectra recorded at 8 K for the four samples implanted with phosphorus (cf. Table V). It can be clearly seen that the two samples implanted with a dose of $6x10^{13}$ cm^{-2} and annealed in N_2/O_2 (black and red curves) exhibit a very similar spectrum, with two broad peaks centered at ~1390 nm and ~1490 nm. The main difference consists in a lower peak intensity for the sample implanted at 150°C (Ph3, red curve) compared to the sample implanted at RT (Ph2, black curve). Assuming that the observed peaks are related to the dislocations observed in TEM as well as to the elongated defects seen in PL imaging maps, this result is in perfect agreement with the reduced implant damage expected when the implant temperature is increased to 150°C. Moreover, the PL spectrum from sample Ph12 implanted with a dose of 2x10^{13} cm^{-2} exhibited the highest band-to-band signal with no other emission peaks throughout the spectrum (blue curve in Figure 15), indicating the absence of defects, in agreement with the PL imaging results (cf. Figure 14 bottom left). Finally, sample Ph18 implanted with a dose of 6x10^{13} cm^{-2} and annealed in N_2 (green curve in Figure 15) shows several low intensity peaks in the 1150-1250 nm range, and a more intense peak centered at 1530 nm.

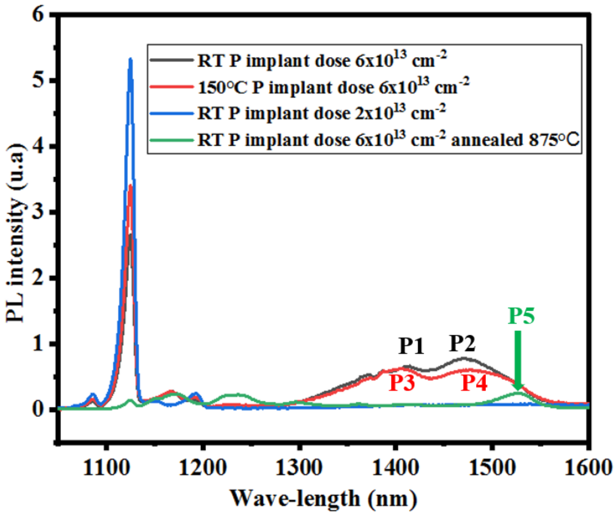

Figure 15: PL spectra taken at a temperature of 8K from samples implanted with P under different conditions (cf. Table V)

Deconvolution analysis was applied in order to determine the main optical emission peaks from all the investigated samples, which are labeled P1/P2 (sample Ph 2), P3/P4 (sample Ph3) and P5 (sample Ph 18) in Figure 15. The corresponding wavelength positions are summarised in Table VI.

Sample no.	Ph 2 - RT implant N_2/O_2 anneal		Ph 3 - 150°C implant N_2/O_2 anneal		Ph 18 - RT implant N_2 anneal
Peak label	P1	P2	P3	P4	P5
wavelength (nm)	1390	1482	1397	1493	1530

Table VI: Peak wavelength positions determined by deconvolution from the samples implanted with Phosphorus under different conditions

We now focus on the on samples Ph2 and Ph3, processed under the same conditions except for the implant temperature. The PL spectra acquired at different temperatures from these two samples are reported in Figure 16. In all cases, the intensity of the emission peaks P1-P4 is found to decrease when increasing the acquisition temperature, which is expected due to thermal broadening. In addition, all the observed peaks are shifted towards higher wavelength at higher acquisition temperatures. Such a common behavior for the four identified peaks suggests that they all originate from defect type.

In previous section, the optical behavior of dislocations was briefly discussed. In particular, it was mentioned that they are generally observed by pairs D1/D2 and D3/D4 [14][27], while the presence of contaminants and/or precipitates located in the vicinity of the dislocations has been shown to play an important role in enhancing or reducing their intensity [14][15]. In our case, the peak pairs observed in each sample (P1/P2 in sample Ph 2 and P3/P4 in sample Ph 3) are located at slightly lower wavelengths (~35 nm) than the D1/D2 lines. This wavelength shift is very close to the one found in previous section for As implants (~38 nm between the observed A1/A2-A3/A4 pairs and the reference S1/S2 lines). This shift might be due to a setup problem that is currently under investigation. However, the wavelength separation between the peaks observed in each sample (P1/P2 in sample Ph 2 and P3/P4 in sample Ph 3) is ~95 nm, which perfectly corresponds to the one reported for the D1/D2 pair (91 nm in [14], 106 nm in [27]). Moreover, the peak evolution as a function of the acquisition temperature (cf. Figure 16) is also consistent with that of the D1/D2 peaks, including the progressive shift towards higher wavelength when the acquisition temperature increases [28]. Considering that, in these samples, dislocations were observed by TEM and elongated defects were imaged in PL maps, it can therefore be concluded that, P1-P4 peaks observed in this work correspond to the D1/D2 lines originating from the dislocations.

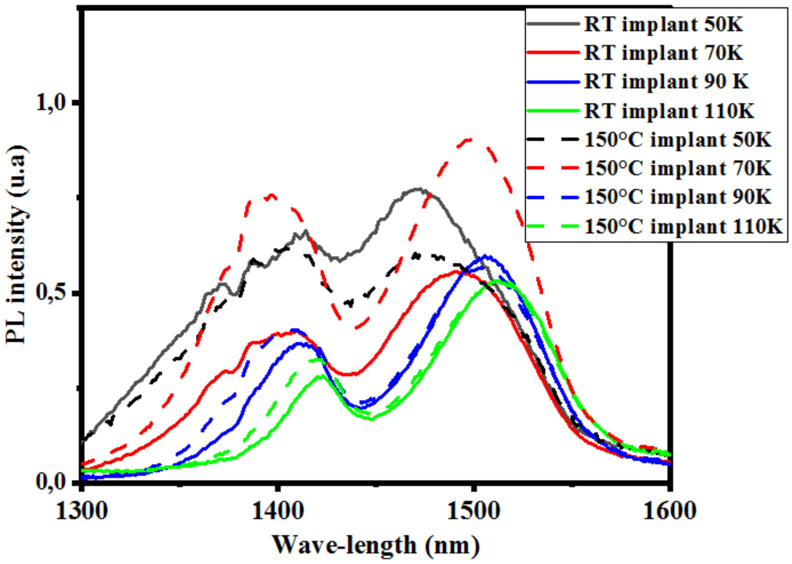

Figure 16: PL spectra acquired at different temperatures from samples Ph2 and Ph3 (cf. Table V) implanted with P at different temperatures (RT and 150°C respectively)

It is interesting to note that samples Ph2 and Ph3 were annealed in an oxygen-reach annealing ambient, which is known to enhance the optical emission from D-lines [27]. In contrast, sample Ph18, annealed in pure nitrogen did not exhibit any peak in the D1/D2 region, the main peak (P5 in table VI) being located at 1530 nm. This result is in agreement with work of Giri et al. who investigated the impact of the annealing ambient on the optical properties of silicon samples implanted with different species, including Al, P and Si ions [17] at doses of 2×10^{14} cm^{-2}. Indeed, the authors found that D1/D2 lines were observed in Al and P implanted samples followed by annealing in pure oxygen ambient, whereas, in the case of a pure nitrogen ambient, no D1/D2 lines were observed and a peak was instead observed at ~1600 nm that the authors attributed to impurity-related precipitates. Due to the lower implant doses investigated in our study (6×10^{13} cm^{-2}), it is unlikely that the P5 peak observed at 1530 nm is related to P precipitates. Further analyses are therefore needed to identify its origin.

5 DoE of B implants into SiGe

As it was mentioned in the Introduction, the results presented in the first three sections of this deliverable are based on implanted Silicon wafers that were available at STMicroelectronics at the beginning of the project. They allowed investigating the impact of the implant temperature on the damage generated during the process, in perfect line with the objectives of this task. However, the annealing processes investigated in these experiments included higher thermal budgets compared to those planned in the MUNDFAB workplan. Since the dedicated SiGe wafers have been fabricated by LETI, it has therefore been possible to design a full set of experiments implying low thermal budgets. In particular, the DoE described below will serve the objectives of both T2.1 and T2.2 tasks.

The details of the selected substrates and implant conditions are summarized in Table VII. 30 Two doping species will be investigated. For p-type doping, B ions will be implanted in Si substrates (wafers 1-3) as well as 30 nm-thick strained SiGe with a Ge content of 20% (wafers 4-6) and 40% (wafers 7-9). The Boron implant energy has been chosen in order to confine the whole dopant profile within the SiGe layers. Three implant temperatures will be investigated: RT, 150°C and 500°C.

For n-type doping, P ions will be implanted only in Si substrates (wafers 10-12). In order to facilitate the comparison between results obtained in the p-type doped wafers, the phosphorus implant energy has been chosen so to have a very similar mean projected range to the one expected for the boron implants.

In the case of RT implants (wafers 1, 4, 7 and 10) two quarters of each wafers will be used for pre-amorphization experiments (PAI, Task 2.2). Two PAI conditions have been selected, aiming at producing either a partial or a full amorphization of the SiGe layers (conditions labeled “Ge PAI 1” and “Ge PAI 2”, respectively).

		Si:B					SiGe(20%):B					SiGe(40%):B					Si:P				
Wafer no.		1			2	3	4			5	6	7			8	9	10			11	12
Wafer part (**a**,**b**: quarter; **c**: half; **f**: full)		a	b	c	f	f	a	b	c	f	f	a	b	c	f	f	a	b	c	f	f
Starting Wafer	Si	x	x	x	x	x											x	x	x	x	x
	s-SiGe 20%						x	x	x	x	x										
	s-SiGe 40%											x	x	x	x	x					
B implant (2 keV, 1x10^{15} cm-2)	Rp: 11 nm	x	x	x	x	x	x	x	x	x	x	x	x	x	x	x					
P implant (6 keV, 1x10^{15} cm-2)	Rp: 12 nm																x	x	x	x	x
Wafer Temperature	RT	x	x	x			x	x	x			x	x	x			x	x	x		
	150°C				x					x					x					x	
	500°C					x					x					x					x
Ge PAI1 (5 keV, 1e15 cm-2)	t(a-Si): ~15 nm		x					x					x					x			
Ge PAI2 (15 keV, 1e15 cm-2)	t(a-Si): ~30 nm			x					x					x					x		
Non-melt LTA (various conditions)																					

Table VII: Details of the high-temperature implant conditions in Si and SiGe wafers for Tasks 2.1 and 2.2

For the experiments dedicated to Task 2.1, multi-pulse non-melt laser annealing will be used to activate the dopants. For each wafer, the threshold energy density for the onset of surface melt, E_{th}, will first be determined experimentally. Then, annealing will be performed with four different laser energy densities below the threshold: E_{th} - 5%, E_{th} - 10%, E_{th} - 15% and E_{th} - 20%. Finally, for each energy density, different number of pulses will be tested, ranging from

1 pulse to 1000 pulses. Similar submelt anneals will also be performed on preamorphized wafers for Task 2.2.

At the date at which this deliverable has been written, all the implants have been performed (HT implants at AMAT, PAI implants at LETI), while the sub-melt anneals are in progress at LETI.

Conclusions

In this deliverable, we reported the results of our investigations about the impact of the wafer temperature on the residual damage remaining after an ion implantation process, as well as on the defects formed during a subsequent annealing step.

In section 1, we discussed the case of self-induced heating during Carbon implantation. We demonstrated that the amorphous thickness could be finely tuned from dozens of nm to less than 5 nm by changing a specific machine-related parameter (i.e. the backside pressure cooling) on a standard industrial implanter. Moreover, the combination of a “homemade” model (for the prediction of the wafer temperature as a function of this specific machine-related parameter) with the KMC simulation code Sentaurus Process (for the evolution of implant-induced damage and amorphous pockets kinetics) results in a perfect prediction of the observed amorphization kinetics in a wide range of implant conditions. These include the super-linear regime (close to the amorphization threshold) as well as the high-dose implants (full amorphization).

In section 2, we investigated the damage evolution following heated implants of Arsenic ions in silicon wafers. We showed experimentally that when the implant temperature is increased from RT to 150°C, an enhanced point defect annihilation occurs during the implant, which prevents the formation of a continuous amorphous layer, while still leaving a considerable level of damage. A further increase of the implant temperature up to 500°C results in an almost perfect structure, with no evidence of amorphous or highly damaged regions. The defects formed after RTA and furnace annealing in these samples were analyzed by TEM and photoluminescence techniques in order to determine their crystallographic nature, their depth position and their optical properties. In particular, it was shown that the optical emission peaks detected by photoluminescence spectroscopy do not originate from the extended defects observed by TEM, but rather from small interstitial clusters formed during the annealing, whose size is below the TEM detection limit. In contrast, in the case of the high-energy Phosphorus implants presented in section 3, a direct correspondence between the photoluminescence emission peaks and the observed elongated dislocations was established. In the next reporting period, KMC and continuum simulations will be implemented to calculate the size distribution of all the defects formed during annealing and estimate the residual population of defect clusters whose size is compatible with the observed PL spectra in both As and P implanted samples.

Finally, in section 4, we described the full set of experiments planned for tasks T2.1 and T2.2 for the investigation of HT implants in conjunction with low-thermal budget anneals. These experiments will be performed on the dedicated SiGe wafers fabricated by LETI, and in collaboration with the privileged partner AMAT.

References

[1] Olson, G. L., & Roth, J. A. (1988). Kinetics of solid phase crystallization in amorphous silicon. *Materials science reports*, *3*(1), 1-77

[2] Colombeau, B., Cowern, N. E. B., Cristiano, F., Calvo, P., Cherkashin, N., Lamrani, Y., & Claverie, A. (2003). Time evolution of the depth profile of {113} defects during transient enhanced diffusion in silicon. *Applied physics letters*, *83*(10), 1953-1955

[3] Hoang, T., Holleman, J., LeMinh, P., Schmitz, J., Mchedlidze, T., Arguirov, T., & Kittler, M. (2007). Influence of dislocation loops on the near-infrared light emission from silicon diodes. *IEEE transactions on electron devices*, *54*(8), 1860-1866

[4] Jain, S. C., Schoenmaker, W., Lindsay, R., Stolk, P. A., Decoutere, S., Willander, M., & Maes, H. E. (2002). Transient enhanced diffusion of boron in Si. *Journal of applied physics*, *91*(11), 8919-8941

[5] Pelaz, L., Marqués, L. A., & Barbolla, J. (2004). Ion-beam-induced amorphization and recrystallization in silicon. *Journal of applied physics*, *96*(11), 5947-5976

[6] Smith, T. C. (1983). Wafer cooling and photoresist masking problems in ion implantation. In *Ion Implantation: Equipment and Techniques* (pp. 196-213). Springer, Berlin, Heidelberg

[7] Sentaurus Process User Guide, 2019.03, Synopsis Inc.

[8] Ashburn, P. (2003). *SiGe heterojunction bipolar transistors* (pp. 152-154). England: John Wiley & Sons

[9] Dumas, P., Duguay, S., Borrel, J., Gauthier, A., Ghegin, E., & Blavette, D. (2019). 3D atomic-scale investigation of carbon segregation in phosphorus co-implanted silicon. *Applied Physics Letters*, *115*(13), 132103

[10] Claverie, A., Bonafos, C., Martinez, A., & Alquier, D. (1996). Interactions between Dopants and End-of-Range Defects in Silicon. In *Solid State Phenomena* (Vol. 47, pp. 195-204). Trans Tech Publications Ltd

[11] K.S. Jones, S. Prussin, E.R. Weber, App. Phys. A 45 (1988) 1-34

[12] "Extended defects in shallow implants", A.Claverie, B.Colombeau, B.de Mauduit, C.Bonafos, X.Hebras, G.Ben Assayag and F.Cristiano, Applied Physics A, 76 (2003) 1025-1033

[13] Duru, R., Le-Cunff, D., Cannac, M., Laurent, N., Dudas, L., Kiss, Z., Cseh, D., Lajtos, I., Jay, F., Nadudvari, G. Photoluminescence for in-line buried defects detection in silicon devices. In *2017 28th Annual SEMI Advanced Semiconductor Manufacturing Conference (ASMC)* (pp. 262-266). IEEE

[14] Arguirov, T., Seifert, W., Kittler, M., & Reif, J. (2002). Temperature behaviour of photoluminescence and electron-beam-induced current recombination behaviour of extended defects in solar grade silicon. *Journal of Physics: Condensed Matter*, *14*(48), 13169

[15] S Pizzini, M Guzzi, E Grilli and G Borionetti, "The photoluminescence emission in the 0.7–0.9 eV range from oxygen precipitates, thermal donors and dislocations in silicon". J. Phys.: Condens. Matter 12 (2000) 10131–10143

[16] Kumar, S. N., Chaussemy, G., Roura, P., & Laugier, A. (1988). Spectroscopic Investigation of Arsenic-Induced Surface Defects in High-Dose As+ Implanted Rapid Thermal Annealed Silicon. *MRS Online Proceedings Library*, *138*(1), 215-220

[17] P. K. Giri, S. Coffa, V. Raineri, V. Privitera, G. Galvagno, A. La Ferla, E. Rimini. "Photoluminescence and structural studies on extended defect evolution during high-temperature processing of ion-implanted epitaxial silicon". J. Appl. Phys. 89 (2001) 4310

[18] Wai Lek Ng, M. A. Lourenço, R. M. Gwilliam, S. Ledain, G. Shao, K. P. Homewood. "An efficient room-temperature silicon-based light-emitting diode", Nature 410 (2001) 192

[19] Giri, P. K. "Photoluminescence signature of silicon interstitial cluster evolution from compact to extended structures in ion-implanted silicon." *Semiconductor science and technology* 20.6 (2005): 638

[20] Yu, Yang, et al. "Photoluminescence evolution in self-ion-implanted and annealed silicon." *Chinese Physics B* 18.11 (2009): 4906

[21] Coffa, Salvatore, Sebania Libertino, and Corrado Spinella. "Transition from small interstitial clusters to extended {311} defects in ion-implanted Si." *Applied Physics Letters* 76.3 (2000): 321-323

[22] Weman H, Monemar B, Oehrleim G S and Jeng S J 1990 *Phys. Rev.* B **42** 3109

[23] Cowern, N. E. B., Mannino, G., Stolk, P. A., Roozeboom, F., Huizing, H. G. A., Van Berkum, J. G. M., et al. (1999). Energetics of self-interstitial clusters in Si. *Physical Review Letters*, *82*(22), 4460

[24] F.Cristiano, B.Colombeau, C.Bonafos, J.Aussoleil, G.Ben Assayag and A.Claverie. “Atomistic simulations of extrinsic defects evolution and transient enhanced diffusion in silicon”. Proceedings of the SISPAD 2001 International Conference, D.Tsoukalas and C.Tsamis ed., Springer-Verlag Wien New York, 2001, p. 30

[25] S Pizzini, M Guzzi, E Grilli and G Borionetti, “The photoluminescence emission in the 0.7–0.9 eV range from oxygen precipitates, thermal donors and dislocations in silicon“. J. Phys.: Condens. Matter 12 (2000) 10131–10143

[26] Joblot, S., Duru, R., Guitard, N., Lu, V., Nassiet, T., Beneyton, R., ... & Pinzelli, L. (2018, September). Characterization of Heated Ion Implantation for non Amorphizing Conditions and Correlation with Kinetic Monte Carlo Simulations. In *2018 22nd International Conference on Ion Implantation Technology (IIT)* (pp. 121-124). IEEE

[27] Steinman, E. A., & Grimmeiss, H. G. (1998). Dislocation-related luminescence properties of silicon. *Semiconductor science and technology*, *13*(1), 124

[28] Tajima, Michio, Hiroshi Takeno, and Takao Abe. "Characterization of point defects in Si crystals by highly spatially resolved photoluminescence." *Materials Science Forum*. Vol. 83. Trans Tech Publications Ltd, 1992